The Astrophysical Journal, 650:L45–L49, 2006 October 10
© 2006. The American Astronomical Society. All rights reserved. Printed in U.S.A.

DUSTY WAVES ON A STARRY SEA: THE MID-INFRARED VIEW OF M31

P. Barmby,[1] M. L. N. Ashby,[1] L. Bianchi,[2] C. W. Engelbracht,[3] R. D. Gehrz,[4] K. D. Gordon,[3] J. L. Hinz,[3] J. P. Huchra,[1] R. M. Humphreys,[4] M. A. Pahre,[1] P. G. Pérez-González,[3] E. F. Polomski,[4] G. H. Rieke,[3] D. A. Thilker,[2] S. P. Willner,[1] and C. E. Woodward[4]

Received 2006 May 22; accepted 2006 August 24; published 2006 September 21

ABSTRACT

Mid-infrared observations of the Andromeda galaxy, M31, obtained with the Infrared Array Camera on board the *Spitzer Space Telescope* are presented. The image mosaics cover areas of approximately $3\overset{\circ}{.}7 \times 1\overset{\circ}{.}6$ and include the satellite galaxies M32 and NGC 205. The appearance of M31 varies dramatically in the different mid-infrared bands, from the smooth bulge and disk of the old stellar population seen at 3.6 μm to the well-known "10 kpc ring" dominating the 8 μm image. The similarity of the 3.6 μm and optical isophotes and the nearly constant optical–mid-infrared color over the inner 400″ confirm that there is no significant extinction at optical wavelengths in M31's bulge. The nuclear colors indicate the presence of dust but not an infrared-bright active galactic nucleus. The integrated 8 μm nonstellar luminosity implies a star formation rate of 0.4 $M_{\odot}$ yr^{-1}, consistent with other indicators that show M31 to be a quiescent galaxy.

Subject headings: galaxies: individual (M31) — galaxies: ISM — galaxies: spiral — galaxies: stellar content — infrared: galaxies

1. INTRODUCTION

The proximity of the Andromeda galaxy, M31, has long made it a prime target for studies of galaxy structure and stellar populations. One technique has been to isolate particular populations; for example, studies of luminous stars (Humphreys et al. 1990) showed that M31 has a lower massive star formation rate than M33 and the LMC. Global studies of particular components have also been valuable: H I maps provide estimates of the mass distribution (Braun & Thilker 2004) and have recently revealed a population of high-velocity clouds (Thilker et al. 2004). ISOPHOT (Haas et al. 1998), the *Midcourse Space Experiment* (*MSX*; Kraemer et al. 2002), and *IRAS* (Habing et al. 1984) observations showed a bright ring of infrared emission with radius 10 kpc coincident with many of the H II regions.

Mapping the entire disk of M31 at mid-infrared wavelengths allows for *both* local and global studies of the galaxy. Observations with the Infrared Array Camera (IRAC; Fazio et al. 2004) on the *Spitzer Space Telescope* simultaneously trace the dust in the spiral arms at 8 μm and the oldest stars in the disk and bulge at 3.6 and 4.5 μm without the complicating extinction or distance effects that make such studies in the Milky Way difficult. IRAC observations of M31 are complemented by deep data now available at many other wavelengths. They also complement *Spitzer* studies of other nearby galaxies.

This Letter presents an initial look at the IRAC observations of M31, focusing on the surface brightness profiles and extended emission. Companion papers discuss longer wavelength Multiband Imaging Photometer for *Spitzer* (MIPS) observations of M31 (Gordon et al. 2006), IRAC and MIPS observations of the M31 satellite galaxy NGC 205 (Marleau et al. 2006), and the implications of the galaxy's morphology as seen in 8 μm nonstellar emission (Block et al. 2006). A distance to M31 of 783 kpc (Stanek & Garnavich 1998) is assumed throughout. All magnitudes are on the Vega system, using the calibration given by Reach et al. (2005).

2. OBSERVATIONS AND DATA REDUCTION

The IRAC observations of M31 were taken as part of *Spitzer* General Observer program 3126 in 2005 January and August.[5] Fifteen Astronomical Observation Requests (AORs) were used to map a region approximately $3\overset{\circ}{.}7 \times 1\overset{\circ}{.}6$ (chosen to match the MIPS observations made as part of program ID 99), with an extension to the northwest (NW) to include NGC 205. The central $1\overset{\circ}{.}6 \times 0\overset{\circ}{.}4$ was covered by three AORs, each having two 12 s frames per position. The outer regions were covered by two AORs, each with two dithered 30 s frames per position. This mapping strategy ensured that observations of each position in the galaxy were separated by at least 2.5 hr, allowing for efficient asteroid rejection in data processing. The complete data set consists of 3000 individual images in each of the IRAC channels.

Data reduction began with the Basic Calibrated Data (BCD) produced by version 11 (for the January data) or version 12 (the August data) of the *Spitzer* Science Center (SSC) pipeline. A "delta dark" offset correction was applied to the 12 s 5.8 μm frames to correct for the first-frame effect, followed by use of the "artifact corrector" software developed by S. Carey, which attempts to remove the electronic effects caused by bright stars. The remaining processing steps were carried out using the "IRAC_proc" software[6] with the 2005 September 5 version of the SSC MOPEX package. The "overlap correction" necessary

[1] Harvard-Smithsonian Center for Astrophysics, 60 Garden Street, MS 65, Cambridge, MA 02138; pbarmby@cfa.harvard.edu, mashby@cfa.harvard.edu, huchra@cfa.harvard.edu, mpahre@cfa.harvard.edu, willner@cfa.harvard.edu.

[2] Astrophysical Sciences, Johns Hopkins University, 3400 North Charles Street, Baltimore, MD 21218; bianchi@pha.jhu.edu, dthilker@pha.jhu.edu.

[3] Steward Observatory, University of Arizona, 933 North Cherry Street, Tucson, AZ 85721; cengelbracht@as.arizona.edu, kgordon@as.arizona.edu, jhinz@as.arizona.edu, pgperez@as.arizona.edu, grieke@as.arizona.edu.

[4] Astronomy Department, School of Physics and Astronomy, University of Minnesota, 116 Church Street, SE, Minneapolis, MN 55455; gehrz@astro.umn.edu, roberta@aps.umn.edu, elwood@astro.umn.edu, chelsea@astro.umn.edu.

[5] A large solar proton event made most of the January data unusable; reobservations were made in August.

[6] IRAC_proc was developed by M. Schuster, M. Marengo, and B. Patten at the Smithsonian Astrophysical Observatory.

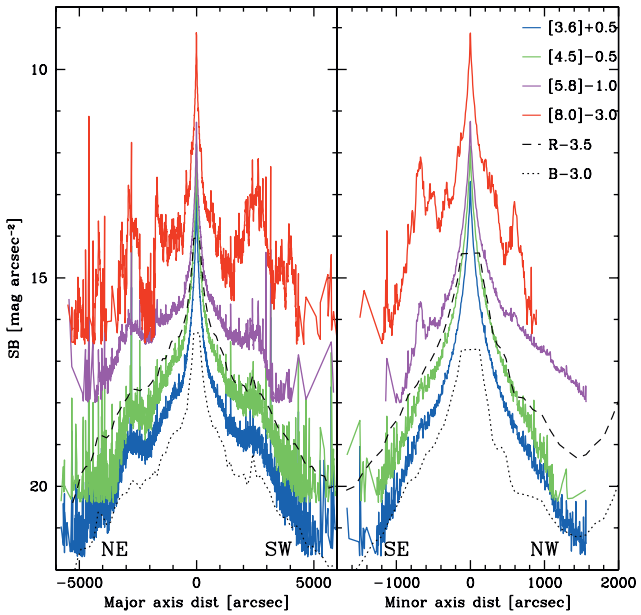

FIG. 2.—Surface brightness profiles measured along the M31 disk major (*left*) and minor (*right*) axes. Profiles have been offset for clarity as indicated in the legend. The mid-infrared profiles are compared to optical profiles from Walterbos & Kennicutt (1987) that are plotted as flat in the center where no data were available. The upturn in the northwest minor-axis profiles of Walterbos & Kennicutt (1987) is due to NGC 205, which is not included in the IRAC images used here.

to make the sky background consistent between frames was computed and applied. Median-combined mosaics of the full data set were created, and then projected into the reference frame of each input BCD image to create "source maps." These source maps were used as the input "uncertainty images" for creating the final photometric mosaics—this step prevents the outlier rejection used by MOPEX from rejecting pixels in bright sources and thereby biasing the photometry. The final mosaics were created with a pixel scale of 0.″86, subsampling the native IRAC pixel scale by a factor of $\sqrt{2}$ to better sample the point-spread function (PSF; FWHM ~ 1.″9). The sky background was removed using the IRAF task IMSURFIT to model the background as a polynomial surface sampled by "blank sky" regions near the edge of the mosaics. After subtraction, the mean image counts in small areas within these regions were computed, and the standard deviation of these means was used to estimate the photometric uncertainties due to the background.

The final step in mosaic production was photometric calibration. Although calibration of point-source photometry varies slightly over the IRAC arrays' field of view (Reach et al. 2005), we did not correct for this since doing so would have corrupted the extended emission. The calibration of IRAC is known to differ between point and extended sources, particularly at 5.8 and 8 μm where a significant fraction of point-source light is scattered on scales comparable to the array size. We used the results of recent work by T. Jarrett (2006, private communication) to correct from point to extended source calibration in the M31 mosaics by multiplying the images by (0.91, 0.94, 0.66, 0.74) in the four IRAC bands, respectively (these values differ slightly from those given in Reach et al. 2005). The standard deviations of the background levels are about 0.04 MJy sr^{-1} in all bands except 5.8 μm, where the background subtraction was more difficult, and the noise was 0.1 MJy sr^{-1} (1 σ). These correspond to limiting surface brightness levels of 21.2, 20.9, 19.0, and 19.6 mag arcsec^{-2} in the four IRAC bands.

The final mosaics are shown in Figure 1 (Plate 1). As with other recent works on IRAC observations of nearby galaxies, we assumed that the 3.6 μm emission is purely due to stars, and we used this to construct maps of the "nonstellar" emission at 5.8 and 8 μm. The stellar emission at these two wavelengths is assumed to correspond to 0.399 and 0.232 times the 3.6 μm emission (Helou et al. 2004). The 8 μm nonstellar image is shown in Figure 1.

3. MORPHOLOGY AND SURFACE BRIGHTNESS PROFILES

M31's appearance changes dramatically over the IRAC bands, in a similar way to other spiral galaxies such as M81 (Willner et al. 2004) and NGC 300 (Helou et al. 2004). The 3.6 μm view is similar to the K_s-band image presented in Jarrett et al. (2003), which is dominated by the bulge, with the spiral arms and disk relatively faint.[7] At 8 μm, M31's bulge is much less prominent, and the spiral arms and the 10 kpc ring are the dominant features. The outer (14 kpc) ring detected at far-infrared wavelengths (Haas et al. 1998; Gordon et al. 2006) and tentatively detected with *MSX* (Kraemer et al. 2002) is also seen in the 8 μm image. The 8 μm image—particularly the nonstellar version—looks extremely similar to the 24 μm image presented by Gordon et al. (2006), showing the same split on the southwest side of the 10 kpc ring that Gordon et al. (2006) attribute to interactions with M32. The "hot spots" seen near the nucleus at 160 μm are also prominent in the 8 μm nonstellar image, where they coincide with the ends of spiral arms.

Disk images 3.°3 × 0.°9 were extracted from the mosaics and used to derive IRAC surface brightness profiles of M31. Peaks of bright stars, a 1′ radius region around M32, and image regions with no coverage were all masked from the profile measurements. Profiles were measured using two methods: making 20″-wide cuts along the disk major and minor axes using the IRAF task PVECTOR, and fitting elliptical isophotes to the images using the ELLIPSE task. Because ELLIPSE can be unstable at low surface brightnesses, the isophote shape parameters (ellipticity, position angle, center) were constrained to be constant beyond the edge of the visible disk at semimajor axes >0.°88. The isophote fit at this distance has an ellipticity ($\epsilon = 1 - b/a$) of 0.73 and a position angle of 38°. Profiles in the three longer wavelength bands were measured on the ellipses fit to the 3.6 μm image, so that colors could be measured at the same spatial locations.

The relative prominence of the M31 disk and bulge in the four IRAC bands is reflected in the major- and minor-axis profiles, shown in Figure 2. Out to a semimajor axis of ~400″ (approximately the edge of M31's bulge), all four bands have very similar profiles. Beyond 400″, the 5.8 and 8.0 μm–band profiles decline more slowly and show more variability due to the clumpy nature of the dust emission. The 10 kpc ring is visible in all of the major-axis profiles; the 8.0 μm profile, in particular, appears highly asymmetric because of the split in the ring. The minor-axis profiles are smoother because they sample mainly the bulge. Both major- and minor-axis profiles are quite similar in shape to the optical profiles presented by Walterbos & Kennicutt (1987), indicating that dust extinction

[7] The 2MASS Large Galaxy Atlas image of M31 is suspected of having an overly faint disk due to problems with background subtraction (T. Jarrett 2006, private communication). We do not compare the IRAC quantitative measurements to those given by Jarrett et al. (2003); instead, we estimate M31's K − [3.6] color by M81's value of 0.3 (Willner et al. 2004).

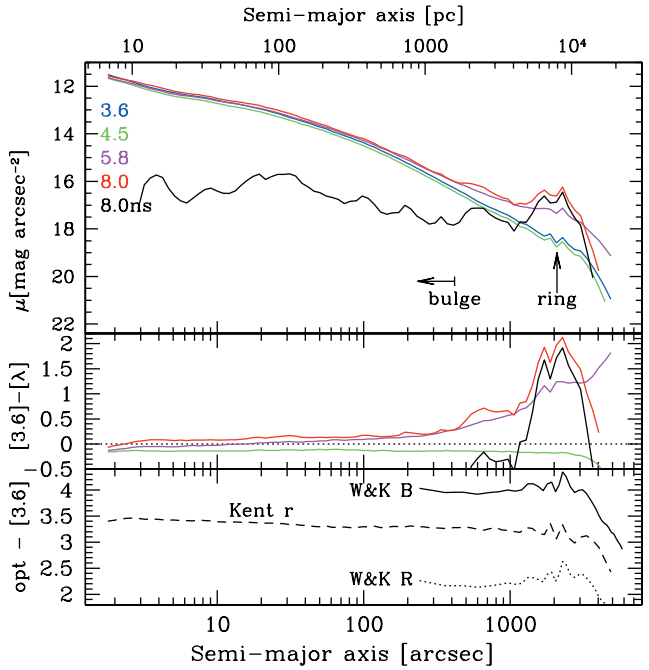

FIG. 3.—Mid-infrared surface brightness and color profiles of M31 derived from IRAF/ELLIPSE isophote fitting. All data use the extended source calibration, as described in the text; "8.0ns" refers to the nonstellar 8 μm image. *Top*: IRAC surface brightness profiles. *Middle*: IRAC color profiles from the same data. *Bottom*: Optical–mid-infrared color profiles, using optical data from Kent (1987) and Walterbos & Kennicutt (1987). The large offset between colors using *r* and *R* is likely due to problems with the zero-point calibration of the Walterbos & Kennicutt (1987) data.

does not have a major effect on the optical profiles. The nucleus of M31 is smaller than the IRAC PSF and does not separate from the bulge emission in the radial profile.

The color profiles of M31 shown in Figure 3 also depict the disk/bulge separation. The median isophote colors within 400″ are $[3.6]-[4.5]=-0.14$, $[3.6]-[5.8]=0.03$, and $[3.6]-[8.0]=0.13$. The $[3.6]-[4.5]$ color is consistent with theoretical expectations for M0 giant stars (see Pahre et al. 2004); the $[3.6]-[5.8]$ and $[3.6]-[8.0]$ colors are slightly redder, presumably because of dust emission. At larger distances, the disk dominates the light, and the colors become redder, particularly at the location of the 10 kpc ring. Comparing the 3.6 μm profile to the *r*-band optical profile of Kent (1987) shows that the $r-[3.6]$ color is nearly constant over the central 400″, with a luminosity-weighted mean of $r-[3.6]=3.41$ mag. This corresponds to $r-K\approx 3.1$, reasonably consistent with the predictions of Maraston (2005). The colors of the M31 nucleus (measured in a 2.″4 radius aperture, with the IRAC point-source calibrations and aperture corrections applied) are $[3.6]-[4.5]=-0.15$, $[3.6]-[5.8]=0.19$, and $[3.6]-[8.0]=0.51$. The red colors at the longer wavelengths suggest that the nucleus has more dust than the bulge, but they are not the very red colors characteristic of an active galactic nucleus (e.g., Stern et al. 2005).

Table 1 gives integrated flux densities and magnitudes of M31 as measured in the largest elliptical isophote ($a=1.^{\circ}8$). The uncertainties in these values include the effects of background variation and a 10% uncertainty in the absolute extended source calibration. The IRAC flux densities are consistent with the *COBE*/DIRBE measurements at 3.5 and 4.9 μm (245 and 128 Jy with 20% uncertainties; Odenwald et al. 1998) and the *MSX* A-band (8.3 μm) value (159 ± 32 Jy; Gordon et

TABLE 1

M31 MID-INFRARED FLUX DENSITIES AND MAGNITUDES

λ (μm)	f_ν (Jy)	$m_{\rm Vega}$
3.6	259 ± 32	0.09 ± 0.13
4.5	144 ± 20	0.24 ± 0.15
5.8	190 ± 35	−0.55 ± 0.20
8.0	151 ± 21	−0.93 ± 0.15
8.0 (nonstellar)	91 ± 21	...

NOTE.—Measurements made in an elliptical aperture of semimajor axis $a=1.^{\circ}8$.

al. 2006). Near–to–mid-infrared colors are another way to check our photometry: Aaronson et al. (1980) measured $H=1.42$ in a 1554″ diameter circular aperture centered on M31. In the same aperture, the 3.6 μm magnitude is 0.84, giving $H-[3.6]=0.58$. Using M81's $K_s-[3.6]\approx 0.3$ (Willner et al. 2004) and the mean $H-K_s=0.27$ measured for early-type (S0/Sa/Sb) spirals by Jarrett et al. (2003), one would predict $H-[3.6]=0.57$, in very good agreement with our measurement.

A model light distribution consisting of an $r^{1/4}$ bulge and an exponential disk were fit to the 3.6 μm semimajor-axis surface brightness (SB) profile. The structural parameters fitted to the disk are sensitive to the inclusion of the ring at semimajor axis lengths $2000'' \le a \le 3500''$, while the bulge effective radius is sensitive to the inner fitting cutoff due to deviations from the idealized $r^{1/4}$ model at $a<100''$ (see Kent 1983). The sky value for the image was determined at isophotes roughly corresponding to 3.5 disk scale lengths. As there is still some galaxy emission at this radius, our sky value is likely overestimated and is probably the dominant cause of the significant reduction in the SB at $a>4000''$ (smaller, but still significant, errors will be present in the profile at $a<4000''$). We chose the fitting regions of $100'' \le a \le 2000''$ and $3500'' \le a \le 4000''$ to minimize these effects, and for consistency with previous work.

The resulting model has (bulge, disk) half-light semimajor-axis lengths of (10.′3 ± 0.′4, 44.′7 ± 0.′6), average ellipticities near to those scale lengths of (0.48 ± 0.02, 0.68 ± 0.04), total magnitudes (0.84 ± 0.13, 0.58 ± 0.06), and an rms of 0.02 mag. The corresponding circularized effective radii are (7.′5 ± 0.′3, 25.′2 ± 0.′7). This disk major-axis scale length of 6.08 ± 0.09 kpc compares well with the longest wavelength (*R*-band) value of 5.9 kpc measured by Walterbos & Kennicutt (1988). The ratio of the bulge effective radius of 1.70 ± 0.07 kpc to the disk scale length places M31 on the upper envelope of local spiral galaxies (de Jong 1996). The fitted bulge and disk models have a flux ratio $B/D=0.78\pm0.11$. This value is biased high relative to the true ratio, however, because the bulge model is too bright at $a<100''$ and the disk model is too faint at the location of the 10 kpc ring. Walterbos & Kennicutt (1988) calculate a similar value in the *R* band.

The model fitting allows for an estimate of M31's total magnitude at 3.6 μm through extrapolation of the disk model to infinite radius. The magnitude within $a<4000$ mag is 0.19 mag, the extrapolated disk from 2.5 scale lengths to infinity adds an additional 0.38 mag, and the sky subtraction errors on the SB profile within this isophote result in an additional 0.15 mag. The implied total magnitude of M31 is therefore −0.34 mag. We have chosen not to quote this model-dependent value in Table 1 for consistency with previous work and our measurements at other wavelengths, but it is consistent with the measurement in the 1.°8 isophote given there when similar corrections are applied. The errors on the total magnitude of M31 are dominated by the systematic error of sky

subtraction on this large galaxy, and less so on the extrapolation of the disk emission.

The 3.6 μm luminosity of M31 can be used to estimate the galaxy's stellar mass. Using a typical value of $B - R = 1.5$ from Walterbos & Kennicutt (1987) and the color-dependent mass-to-light ratios of Bell & de Jong (2001), an estimated M/L_K for M31 is about 1.15 in solar units. Using $K - [3.6] = 0.3$ and multiplying by M/L_K, the resulting stellar mass is $1.6 \times 10^{11}\ M_\odot$. Recent dynamical mass estimates of the M31 disk+bulge (e.g., Widrow et al. 2003; Geehan et al. 2006) are $\sim 10^{11}\ M_\odot$, in reasonable agreement with this derived stellar mass. Asymptotic giant branch (AGB) stars can be important contributors to the total near-infrared luminosities of galaxies (Maraston 2005). However, the most luminous AGB stars are predicted by Groenewegen (2006) to have much redder colors ($0.5 < [3.6] - [4.5] < 1$) than observed for M31, so we conclude that they do not dominate M31's 3.6 μm luminosity.

The 8 μm nonstellar emission is dominated by the 7.7 μm polycyclic aromatic hydrocarbon band, which is a useful though imperfect star formation rate (SFR) indicator. It is therefore instructive to compare the M31 8 μm luminosity with other star formation indicators, such as Hα, radio, and total infrared luminosities, and with these values for other galaxies. Wu et al. (2005) derived a calibration for SFR as a function of 8 μm nonstellar luminosity νL_ν[8 μm(dust)] (hereafter L_8) using correlations between L_8 and L(Hα) and L(1.4 GHz). The IRAC 8 μm nonstellar flux density measured for M31 corresponds to a luminosity of $\log (L_8/L_\odot) = 8.8$. The Wu et al. (2005) calibration yields an SFR of $0.4\ M_\odot\ \mathrm{yr}^{-1}$.

It is possible to compare M31's 8 μm–derived SFR with SFRs from other indicators, but since all such indicators have calibration uncertainties (e.g., the Wu et al. 2005 8 μm/SFR calibration is based on a small number of galaxies with a limited range of properties), we instead compare the observed properties directly. To estimate the Hα luminosity of M31, we convert the value given by Devereux et al. (1994) to the 780 kpc distance, multiply by 0.8 to account for [N II] contamination, and multiply by 3.4 (as done by Walterbos & Braun 1994) to correct for extinction. The resulting $L(\mathrm{H}\alpha) = 2.6 \times 10^7\ L_\odot$, which predicts $\log (L_8/L_\odot) = 9.1$. The 1.4 GHz radio flux density measured by Beck et al. (1998), $3.34 \times 10^{20}\ \mathrm{W\ Hz}^{-1}$, yields a predicted $\log (L_8/L_\odot) = 8.4$. Figure 12 of Dale et al. (2005) gives the ratio of νf_ν[8 μm(dust)]/f(3–1100 μm) as a function of $f_\nu(70\ \mu\mathrm{m})/f_\nu(160\ \mu\mathrm{m})$ for SINGS galaxies. From Gordon et al. (2006), M31 has $f(70)/f(160) = 0.12$, with the corresponding $f(3\text{–}1100\ \mu\mathrm{m}) = 2.57 \times 10^{-10}\ \mathrm{W\ m}^{-2}$, yielding a predicted $\log (L_8/L_\odot) = 9.0$. The Hα and far-infrared predictions are in reasonably good agreement and are consistent with the observed 8 μm luminosity given the scatter in the relationships. The 8 μm luminosity predicted from the radio flux is lower than observed, perhaps indicating that some extended emission was resolved out of the radio maps. All of the "star formation" luminosities are at the low end of the galaxy distribution. Despite its prominent star-forming ring, M31 is a predominantly quiescent galaxy.

We thank the referee for helpful suggestions. This work is based on observations made with the *Spitzer Space Telescope*, which is operated by the Jet Propulsion Laboratory, California Institute of Technology under a contract with NASA. Support for this work was provided by NASA through an award issued by JPL/Caltech.

Facilities: Spitzer(IRAC)

REFERENCES

Aaronson, M., Mould, J., & Huchra, J. 1980, ApJ, 237, 655
Beck, R., Berkhuijsen, E. M., & Hoernes, P. 1998, A&AS, 129, 329
Bell, E. F., & de Jong, R. S. 2001, ApJ, 550, 212
Block, D. L., et al. 2006, Nature, in press
Braun, R., & Thilker, D. A. 2004, A&A, 417, 421
Dale, D. A., et al. 2005, ApJ, 633, 857
de Jong, R. S. 1996, A&A, 313, 45
Devereux, N. A., Price, R., Wells, L. A., & Duric, N. 1994, AJ, 108, 1667
Fazio, G. G., et al. 2004, ApJS, 154, 10
Geehan, J. J., Fardal, M. A., Babul, A., & Guhathakurta, P. 2006, MNRAS, 366, 996
Gordon, K. D., et al. 2006, ApJ, 638, L87
Groenewegen, M. A. T. 2006, A&A, 448, 181
Haas, M., Lemke, D., Stickel, M., Hippelein, H., Kunkel, M., Herbstmeier, U., & Mattila, K. 1998, A&A, 338, L33
Habing, H. J., et al. 1984, ApJ, 278, L59
Helou, G., et al. 2004, ApJS, 154, 253
Humphreys, R. M., Massey, P., & Freedman, W. L. 1990, AJ, 99, 84
Jarrett, T. H., Chester, T., Cutri, R., Schneider, S. E., & Huchra, J. P. 2003, AJ, 125, 525
Kent, S. M. 1983, ApJ, 266, 562
Kent, S. M. 1987, AJ, 94, 306
Kraemer, K. E., Price, S. D., Mizuno, D. R., & Carey, S. J. 2002, AJ, 124, 2990
Maraston, C. 2005, MNRAS, 362, 799
Marleau, F. R., Noriega-Crespo, A., Misselt, K., Gordon, K., Engelbracht, C., Rieke, G., Barmby, P., & Willner, S. P. 2006, ApJ, 646, 929
Odenwald, S., Newmark, J., & Smoot, G. 1998, ApJ, 500, 554
Pahre, M. A., Ashby, M. L. N., Fazio, G. G., & Willner, S. P. 2004, ApJS, 154, 229
Reach, W. T., et al. 2005, PASP, 117, 978
Stanek, K. Z., & Garnavich, P. M. 1998, ApJ, 503, L131
Stern, D., et al. 2005, ApJ, 631, 163
Thilker, D. A., Braun, R., Walterbos, R. A. M., Corbelli, E., Lockman, F. J., Murphy, E., & Maddalena, R. 2004, ApJ, 601, L39
Walterbos, R. A. M., & Braun, R. 1994, ApJ, 431, 156
Walterbos, R. A. M., & Kennicutt, R. C., Jr. 1987, A&AS, 69, 311
———. 1988, A&A, 198, 61
Widrow, L. M., Perrett, K. M., & Suyu, S. H. 2003, ApJ, 588, 311
Willner, S. P., et al. 2004, ApJS, 154, 222
Wu, H., Cao, C., Hao, C.-N., Liu, F.-S., Wang, J.-L., Xia, X.-Y., Deng, Z.-G., & Young, C. K.-S. 2005, ApJ, 632, L79

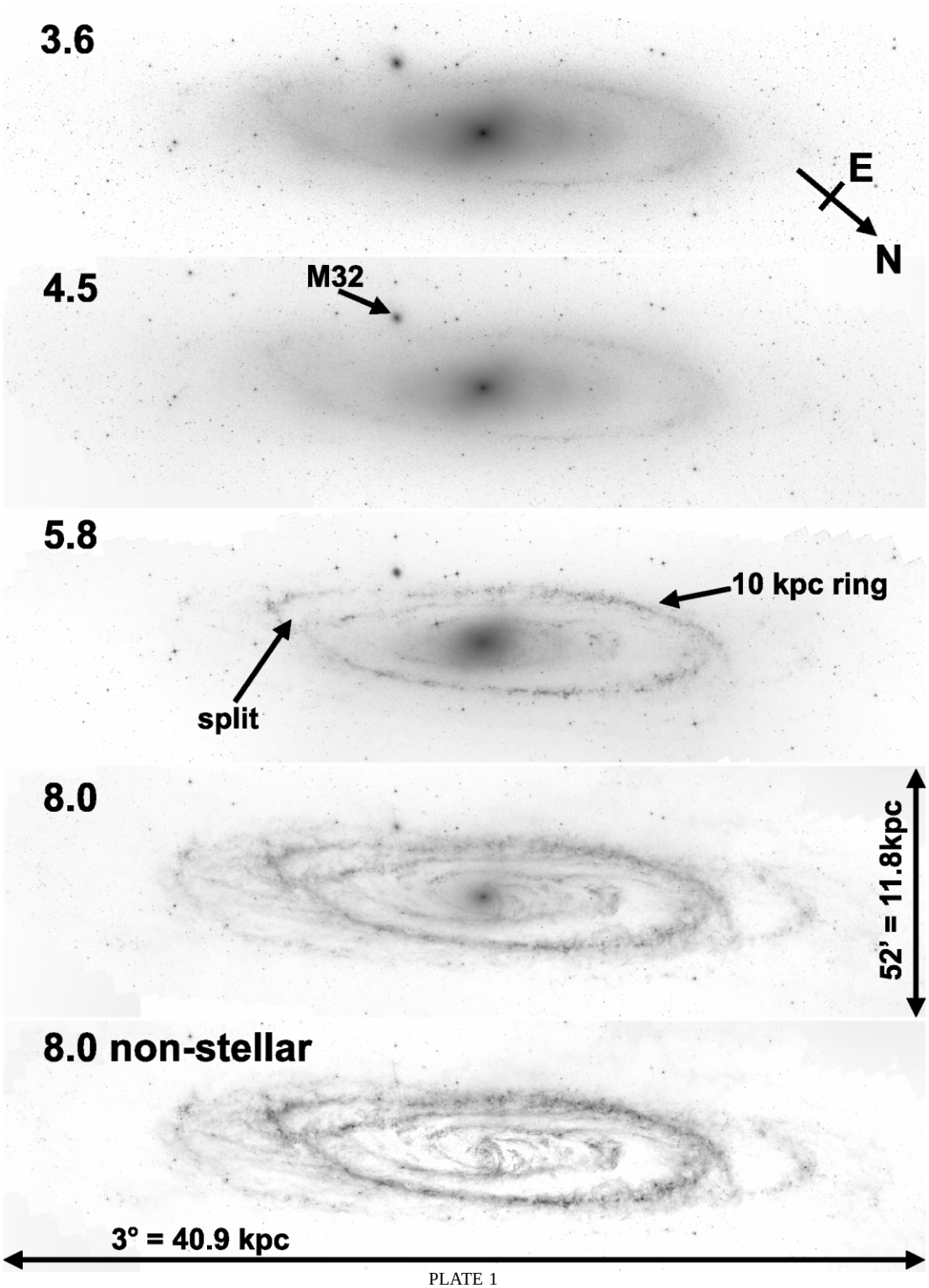

PLATE 1

FIG. 1.—Mid-infrared mosaics of M31 as seen in the IRAC bands. The gray scales are approximately logarithmic with intensity. *From top to bottom*: 3.6, 4.5, 5.8, 8, and 8 μm nonstellar (produced by subtracting the expected stellar contribution to this band, a scaled version of the 3.6 μm image). All images are centered on the nucleus and cover an area of $3\overset{\circ}{.}0 \times 0\overset{\circ}{.}87$. NGC 205 was observed with IRAC but is not shown here (see Marleau et al. 2006).